2026 IEEE International Conference on Robotics and Automation (ICRA 2026)
June 1-5, 2026. Vienna, Austria

Stability-Aware Banked Turn Maneuver Control and Command Augmentation for 2-DOF Pendulum-Driven Spherical Robots

Derek J. Pravecek, Rishi V. Jangale, Aaron Villanueva, Robert O. Ambrose (*IEEE Member*)

***Abstract*— Executing banked turns at elevated speeds poses significant dynamic challenges for 2-DOF pendulum-driven spherical robots. A steady-state torque balance reveals that centripetal loading at high speeds limits feasible roll angles and demands increasingly aggressive pendulum actuation. We derive a closed-form expression for the required pendulum angle and integrate this into a bank-aware Command Augmentation System (CAS) and control law that automatically alters infeasible commands. Experimental tests on Texas A&M RAD Lab's RoboBall II platform demonstrate that the CAS-equipped bank controller enables stable bank maneuvers at speeds up to 6 rad/s (1.83 m/s), where previous controllers fail, by dynamically limiting roll commands based on velocity and internal pressure.**

***Index Terms*— Nonholonomic Mechanisms and Systems; Constrained Motion Planning; Field Robots**

I. INTRODUCTION

The steering mechanics of pendulum-driven spherical robots resemble both fixed-wing aircraft executing banked turns and ground vehicles experiencing tire-limited oversteer or understeer. In all cases, a centripetal force is needed to sustain curved motion. For aircraft, this force comes from the horizontal component of lift during a bank; for ground vehicles, it is produced by lateral tire forces or, on banked roads, by the horizontal component of the normal force.

Similarly, a spherical robot relies on the frictional no-slip constraint at its ground contact point to generate centripetal force. Kinematically, its turning behavior is similar to that of an aircraft: the robot rolls to an angle ϕ and follows a circular trajectory as long as forward propulsion F_t is maintained. This analogy is illustrated in Fig. 1. However, the source of centripetal force is more comparable to a ground vehicle, where tire-ground interaction generates the necessary lateral force as shown in Fig. 2 alongside the robot's contact-driven turning behavior.

Vehicles with complex dynamics, such as pendulum-driven spherical robots, must account for their physical limitations, even when the operator is not fully aware of those constraints across the robot's state space. For example, race car drivers must steer more aggressively at higher speeds to overcome increasing inertial forces, requiring precise control to avoid instability. In the aerospace domain, aircraft like the YF-16 address this challenge using command augmentation systems (CAS), which interpret pilot inputs and translate them into feasible control actions that ensure stability [1]. To the best of our knowledge, this type of dynamic-aware autonomy has not yet been explored in the context of spherical robot control architectures.

**Research supported by the Texas A&M Chancellor's Research Initiative and matching funds from the Texas Governor's University Research Initiative.

Authors are with Texas A&M University, College Station TX, 77843 USA
D. Pravecek's e-mail is derekprav17@tamu.edu

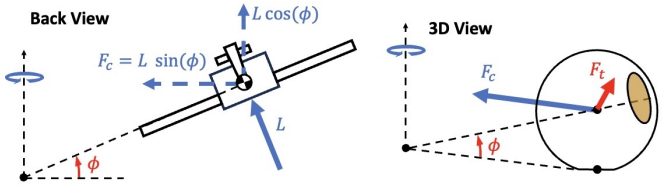

Fig. 1. The banked turn of a fixed-wing aircraft (left) is kinematically similar to that of a spherical robot (right).

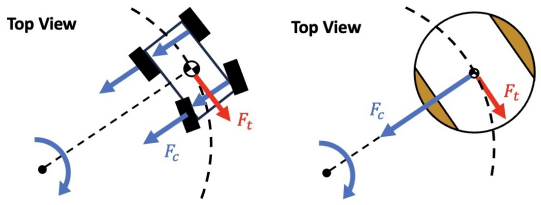

Fig. 2. The centripetal force of a turning wheeled ground vehicle (left) is similar to that of a spherical robot (right) due to its ground contact.

Zhang et al. [2] propose a hybrid A* path planning method for pendulum-driven spherical robots, using a kinematic model to generate feasible state trajectories. However, their approach does not consider the centripetal loading experienced by the robot and its pendulum during high-speed maneuvers, which fundamentally limits the robot's turning capability at elevated drive velocities. In contrast, Nagai et al. [3] and Belzile et al. [4] explicitly include centrifugal forces in their dynamic models, yet they do not analyze how these fictitious forces influence the robot's steering authority at speed. Machmudah et al. [5] develop a bank-aware trajectory planner for fixed-wing UAVs, incorporating banking-related dynamic constraints into the planning process. A similar dynamics-aware planning framework could be extended to spherical robots, provided that their internal dynamics and performance limitations are better characterized.

To date, no prior work has addressed the challenge of accounting for dynamic centripetal loading in pendulum-driven spherical robots performing banked maneuvers. Previous work in [6] models and compensates the quasi-static resistive torque generated by soft-shell deformation at the ground contact patch. That formulation assumes the robot operates at low speeds where shell deformation dominates the steering dynamics and velocity-dependent inertial loading can be neglected. In contrast, this paper investigates the high-speed regime in which centripetal and centrifugal effects become dominant contributors to the steering torque balance. The

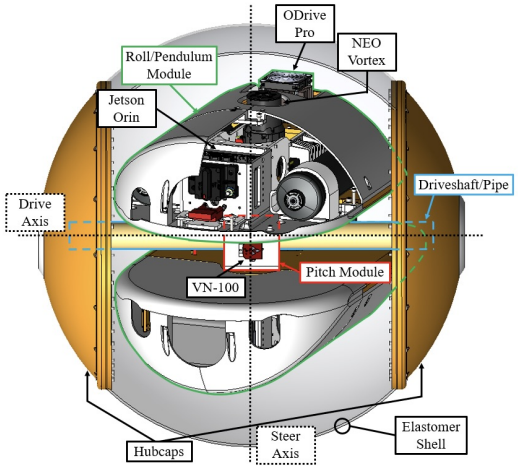

Fig. 3. Critical components and subsystems of a 0.61 m diameter soft-shell spherical robot platform, highlighting the internal pendulum and pitch module.

analysis focuses on the steady-state condition of a banked maneuver, which reveals the pendulum torque and angle required to maintain a turn for a given roll angle and drive shaft speed. This steady-state formulation is particularly useful because it exposes whether a commanded maneuver is physically achievable: if the required pendulum angle exceeds the robot's mechanical limits, the maneuver cannot be sustained regardless of the controller design.

By systematically deriving the internal force and moment balances and incorporating the empirical flat torque model, we obtain a closed-form expression for the steady-state pendulum angle required to sustain a given roll angle and drive shaft speed. This reveals speed-dependent limitations on turning behavior that constrain the robot's maneuverability at higher velocities. Building on this result, we introduce a bank-aware control law that compensates for centripetal and gravitational loading, together with a real-time Command Augmentation System (CAS) that modifies roll and pendulum commands to enforce dynamically feasible steering limits and prevent the robot from entering unstable or physically infeasible turning regimes.

II. BACKGROUND

Pendulum-driven spherical robots typically consist of three primary links: the shell, the pitch center, and the pendulum. Each link has an associated mass, denoted m_s, m_{pc}, and m_p for the shell, pitch center, and pendulum, respectively. The shell has radius R, defined as the distance from its geometric center $\mathbf{c}$ to its outer surface. The centers of gravity (c.g.) of the pitch center and pendulum are located at distances r_{pc} and r_p from $\mathbf{c}$, respectively. These parameters are illustrated in Fig. 4.

The pitch center and pendulum together form the robot's internal chassis, which houses the avionics and actuators. In contrast, the shell functions as a spherical *wheel* that encloses the chassis. A labeled diagram of the pendulum-driven spherical robot named RoboBall II is shown in Fig. 3. RoboBall II is the Texas A&M RAD Lab's 0.61 m diameter, 42 kg spherical robot platform. The onboard avionics include

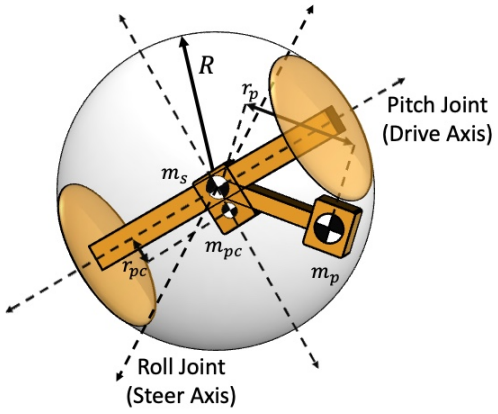

Fig. 4. A diagram depicting a 2-DOF pendulum-driven spherical robot's relevant parameters.

motor controllers, a Jetson Orin Nano computer, a WiFi router, a VN-100 IMU for measuring the shell's orientation, and absolute encoders for measuring the relative steering angle θ between the pendulum and the shell.

The robot rolls about its forward axis when the pendulum swings laterally, and the actuator between the two internal joints applies a torque to the shell. By Newton's third law, an equal and opposite torque is applied to the pendulum. This interaction enables the robot to steer side-to-side. Forward acceleration occurs when the pitch center and pendulum rotate about the drive axis.

This work focuses on the **steady-state** behavior of the robot during banking maneuvers. Under the steady-state assumption, the pitch angle of the internal mechanism is taken to be zero. Consequently, no forward acceleration is necessary to maintain the motion.

A. Orientation Definitions

The shell's orientation is described using a 3-1-2 Euler angle sequence, defined through a series of virtual and body-fixed coordinate frames. The **inertial frame**, denoted $\{x_0, y_0, z_0\}$, serves as the global reference. A yaw rotation ψ about the z_0 axis defines the **robot frame** $\{x_r, y_r, z_r\}$. A subsequent roll rotation ϕ about the x_r axis produces the **ball frame** $\{x_b, y_b, z_b\}$, as shown in Fig. 5. These two frames are *virtual chassis frames*—they are not rigidly attached to any physical link, but are used to simplify the description of the shell's orientation, which continuously rotates about its drive axis.

The **pendulum frame** $\{x_p, y_p, z_p\}$ is a body-fixed frame attached to the pendulum. It is defined by the pendulum roll angle θ, which rotates about the x_b axis of the ball frame. The global angle that the pendulum makes with respect to the inertial z_0 axis is denoted θ_g, and its relationship to ϕ and θ is given in (1).

$$\theta_g = \phi + \theta \tag{1}$$

B. Differential Kinematics

The angular velocity of the **ball frame** is given in (2), derived from the kinematic relationships illustrated in Fig. 6. Similarly, the angular velocity of the shell, expressed in the

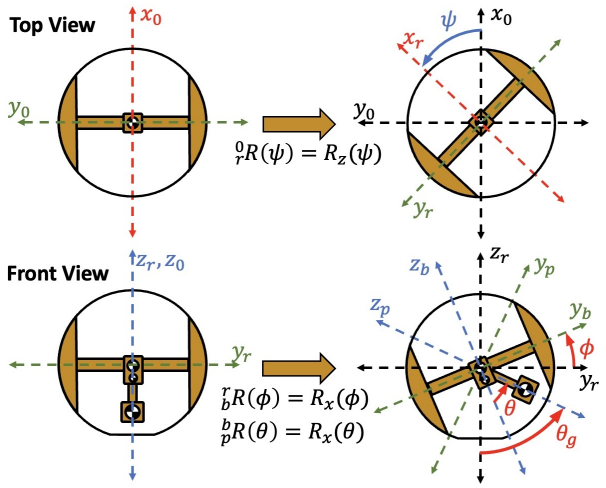

Fig. 5. The sequential yaw and roll rotation angle and coordinate frames used to define the spherical robot and pendulum's 3D orientation.

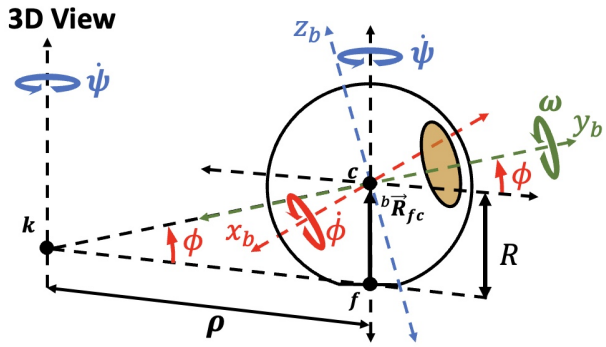

Fig. 6. An angular velocity-based kinematic diagram of the **ball frame** and shell link.

ball frame, is defined in (3) by introducing the shell's angular speed about its drive axis, denoted ω.

$$ {}^{b}\vec{\boldsymbol{\omega}}_b = \begin{pmatrix} \dot{\phi} \\ \dot{\psi}\sin(\phi) \\ \dot{\psi}\cos(\phi) \end{pmatrix} \tag{2} $$

$$ {}^{b}\vec{\boldsymbol{\Omega}}_s = \begin{pmatrix} \dot{\phi} \\ \dot{\psi}\sin(\phi) + \omega \\ \dot{\psi}\cos(\phi) \end{pmatrix} \tag{3} $$

When the robot rolls to the side while simultaneously driving forward, it executes a yaw motion about the center of curvature $\mathbf{k}$, where the driveshaft contacts the ground. This motion is also depicted in Fig. 6, where ρ represents the radius of curvature of the robot's trajectory. The robot's radius R and the trajectory's radius of curvature ρ form a right triangle, which provides the geometric basis for the expression for ρ given in (4).

$$ \rho = \frac{R}{\tan(\phi)} \tag{4} $$

Fig. 7 illustrates a top-down view of the robot executing a banked maneuver, wherein the shell is rolled to a non-zero angle ϕ while the robot drives forward at velocity v_{sx}. The robot's forward velocity is related to its heading rate

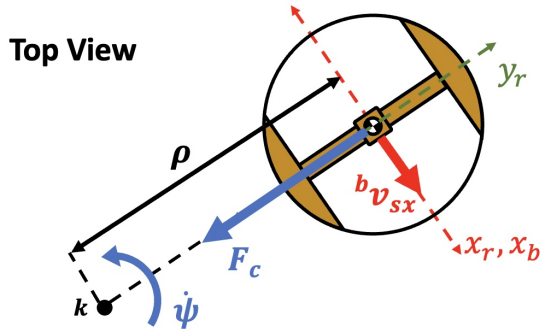

Fig. 7. Top view of the robot turning about its center of curvature $\boldsymbol{k}$ represented in the **robot frame**

$\dot{\psi}$ via the no-slip constraint at the ground contact point $\mathbf{f}$, as defined in (5). These relationships establish a direct connection between the robot's roll angle, drive speed, and yaw rate—highlighting a fundamental coupling at the core of the robot's banking dynamics. A more detailed treatment of this relationship is provided in [7].

$$ \begin{aligned} {}^{b}\vec{v}_{sx} = -\rho\dot{\psi} &= R\cos(\phi)\omega \\ \dot{\psi} &= -\sin(\phi)\omega \end{aligned} \tag{5} $$

III. Steady State Centripetal Loading Aware Steering Model

This section derives the steady-state dynamics of the steering system, emphasizing the centripetal loading experienced by each link during a banking maneuver at nonzero speed. The objective is to determine the torque—and thus the pendulum angle—required to sustain a steady turn while the robot operates at a given drive shaft speed ω. This is accomplished by applying Newton's translational and Euler's rotational equations of motion (EOMs). Fig. 8 presents the Free Body Diagrams (FBDs) for the steering system, illustrating the relevant forces acting on both the shell/pitch center and the pendulum.

This formulation assumes the internal mechanism does not pitch, and that the pitch center is effectively rigidly attached to the **ball frame**, yielding ${}^{b}\vec{\boldsymbol{\omega}}_{pc} = {}^{b}\vec{\boldsymbol{\omega}}_b$. This simplifies the dynamics and is justified by empirical observations showing negligible pendulum pitch during quasi-steady-state motion. The resulting centripetal force on each link element i is given by (6).

$$ F_{c,i} = \frac{m_i\, {}^{b}v_{sx}^2}{\rho} = m_i R\omega^2\cos(\phi)\sin(\phi) \tag{6} $$

The term τ_{flat}, illustrated in Fig. 8, represents the nonlinear *stiffness* torque exerted on the soft shell due to deformation at the ground contact point, which shifts as the robot rolls to nonzero angles. Reference [6] investigates this effect and introduces the *fingerprint method* for characterizing soft-shell deformation. This method empirically models τ_{flat} as a function of the robot's roll angle ϕ and internal pressure P, using the Spherical Soft-Shell Magic Formula (S^3MF). The resulting empirical model is used as a feedforward term

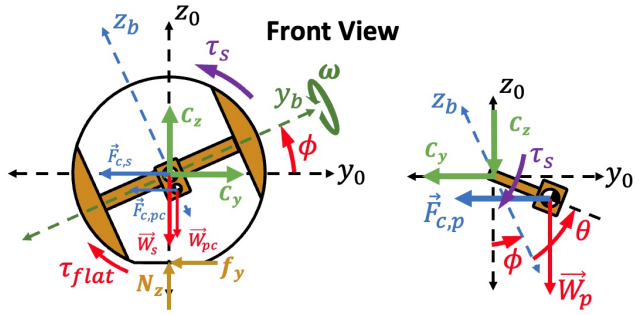

Fig. 8. The FBD of the robot's shell and pitch center (left) and pendulum (right) depicting the internal forces, the soft-shell's opposing torque and forces, the centripetal loading induced by banking, and the steering actuator's shared torque.

in a control scheme to improve the roll-setpoint tracking performance of soft-shell spherical robots [6].

However, that work neglects the centripetal loading experienced by the robot during high-speed locomotion, operating under the assumption that τ_{flat} is the dominant resistive torque acting on the shell. As demonstrated in Section IV-A, this assumption breaks down at elevated speeds where dynamic loading effects—most notably centripetal and centrifugal torques—begin to dominate the system's behavior, as further detailed in Subsection III-D.

A. Steady-State System Force Balance

The steady-state (denoted ss) translational force balance acting on the pendulum along the y-axis is defined in (7), where C_y is the internal force that acts between the shell and pendulum and $F_{c,p}$ is the centripetal force experienced by the pendulum. Similarly, the shell/pitch center's steady-state translational force balance is defined in (8). The ground frictional force f_y is obtained by combining (7) and (8) and will be used in the subsequent moment balance equations.

$$\left(\sum {}^{b}\vec{\mathbf{F}}_{p}\right)_{y,ss} = 0 = -C_y - F_{c,p} \tag{7}$$

$$\left(\sum {}^{b}\vec{\mathbf{F}}_{s/pc}\right)_{y,ss} = 0 = f_y + C_y - F_{c,s} - F_{c,pc} \tag{8}$$

B. Shell/Pitch Center Balance of Moments

The shell/pitch center's moment balance using Euler's rotational equations for rigid-body motion is defined in (9), where the mass moment of inertia tensors of the shell and pitch center are defined below. The inertial terms from the left-hand side of Euler's formula are important and will contribute to the steady-state dynamics. These inertial contributions are typically thought of as the fictitious centrifugal forces acting on the system, meaning they are not actual physical forces acting on the robot but rather a result of inertia.

$$\begin{aligned}&\left({}^{b}\mathbf{I}_s\,{}^{b}\dot{\vec{\mathbf{\Omega}}}_s + \left({}^{b}\vec{\boldsymbol{\omega}}_b \times {}^{b}\mathbf{I}_s\,{}^{b}\vec{\mathbf{\Omega}}_s\right)\right)_{x,ss}\\ &+\left({}^{b}\mathbf{I}_{pc}\,{}^{b}\dot{\vec{\boldsymbol{\omega}}}_b + \left({}^{b}\vec{\boldsymbol{\omega}}_b \times {}^{b}\mathbf{I}_{pc}\,{}^{b}\vec{\boldsymbol{\omega}}_b\right)\right)_{x,ss}\\ &=\left(\sum {}^{b}\vec{\mathbf{N}}_{s/pc}\right)_{x,ss}\end{aligned} \tag{9}$$

where

$${}^{b}\dot{\vec{\mathbf{\Omega}}}_{s,ss} = \begin{pmatrix}\omega^2\cos(\phi)\sin(\phi)\\0\\0\end{pmatrix},\quad {}^{b}\mathbf{I}_s = \begin{bmatrix}I_{sx}&0&0\\0&I_{sy}&0\\0&0&I_{sz}\end{bmatrix}$$

$${}^{b}\dot{\vec{\boldsymbol{\omega}}}_{b,ss} = \begin{pmatrix}0\\0\\0\end{pmatrix},\quad {}^{b}\vec{\boldsymbol{\omega}}_{b,ss} = \begin{pmatrix}0\\-\omega\sin^2(\phi)\\-\omega\cos(\phi)\sin(\phi)\end{pmatrix}$$

$${}^{b}\vec{\mathbf{\Omega}}_{s,ss} = \begin{pmatrix}0\\\omega\cos^2(\phi)\\-\omega\cos(\phi)\sin(\phi)\end{pmatrix}$$

$${}^{pc}\mathbf{I}_{pc} = \begin{bmatrix}I_{pcx}+m_{pc}r_{pc}^2&0&0\\0&I_{pcy}+m_{pc}r_{pc}^2&0\\0&0&I_{pcz}\end{bmatrix}$$

Equation (10) shows what terms are left after applying the steady-state assumption to the LHS of (9).

$$\begin{aligned}&\left(I_{sx}+I_{sy}\right)\omega^2 c(\phi)s(\phi)\\ &+\left(\left(I_{sz}+I_{pcz}-\left(I_{sy}+I_{pcy}+m_{pc}r_{pc}^2\right)\right)\omega^2 c(\phi)s^3(\phi)\right)\\ &=\left(\sum {}^{b}\vec{\mathbf{N}}_{s/pc}\right)_{x,ss}\end{aligned} \tag{10}$$

Equation (11) defines the RHS of (9) where W_{pc} is the weight of the pitch center. Substituting the result combining (7) and (8) into f_y yields the complete RHS defined in (12).

$$\begin{aligned}\left(\sum {}^{b}\vec{\mathbf{N}}_{s}\right)_{x,ss} &= \tau_s - \tau_{\text{flat}} - f_y R\\ &\quad - F_{c,pc}\,r_{pc}c(\phi) - W_{pc}r_{pc}s(\phi)\end{aligned} \tag{11}$$

$$\begin{aligned}\left(\sum {}^{b}\vec{\mathbf{N}}_{s/pc}\right)_{x,ss} &= \tau_s - \tau_{\text{flat}}\\ &\quad - (F_{c,s}+F_{c,pc}+F_{c,p})R\\ &\quad - F_{c,pc}\,r_{pc}c(\phi) - m_{pc}r_{pc}g s(\phi)\end{aligned} \tag{12}$$

Finally, combining (10) and (12) and substituting the element-based centripetal force defined in (6) yields the steady-state torques that act on the shell defined below in (13) where all terms other than the actuator's torque is moved to the LHS. This equation is equated to T_{shell} to make later substitution simpler.

$$\begin{aligned}&\underbrace{\left(I_{sx}+I_{sy}\right)\omega^2\cos(\phi)\sin(\phi)}_{\text{Centrifugal Torque } C_{fs}}\\ &+\underbrace{\left[(m_s+m_{pc}+m_p)R^2+m_{pc}r_{pc}R\cos(\phi)\right]\omega^2 c\phi s\phi}_{\text{Centripetal Torque } C_s}\\ &+\underbrace{\left[I_{sz}+I_{pcz}-\left(I_{sy}+I_{pcy}+m_{pc}r_{pc}^2\right)\right]\omega^2\cos(\phi)\sin^3(\phi)}_{\text{Gyroscopic Coupling } N_s}\\ &+\underbrace{m_{pc}r_{pc}g\sin(\phi)}_{\text{Gravitational Torque}}+\underbrace{\tau_{\text{flat}}}_{\text{Shell Flat Torque}} = \underbrace{\tau_s}_{\text{Actuator Torque}} = T_{\text{shell}}\end{aligned} \tag{13}$$

C. Pendulum Balance of Moments

The moment balance process is repeated for the pendulum shown on the right of Fig. 8 where its sum of torques is defined in (14). Here, it can be observed that the steady-state angular velocity of the pendulum in the **ball frame** is the same as the steady-state angular velocity of the **ball frame** expressed in the **ball frame**.

$$\begin{aligned}&\left({}^{b}\mathbf{I}_p\,{}^{b}\dot{\vec{\boldsymbol{\omega}}}_p + \left({}^{b}\vec{\boldsymbol{\omega}}_b \times {}^{b}\mathbf{I}_p\,{}^{b}\vec{\boldsymbol{\omega}}_p\right)\right)_{x,ss} \\ &= -\tau_s - W_p r_p s(\phi+\theta) - F_{c,p} r_p c(\phi+\theta)\end{aligned} \tag{14}$$

where

$${}^{b}\dot{\vec{\boldsymbol{\omega}}}_{p,ss} = \begin{pmatrix}0\\0\\0\end{pmatrix}, \quad {}^{b}\vec{\boldsymbol{\omega}}_{p,ss} = \begin{pmatrix}0\\-\omega\sin^2(\phi)\\-\omega\cos(\phi)\sin(\phi)\end{pmatrix}$$

$${}^{p}\mathbf{I}_p = \begin{bmatrix} I_{px}+m_p r_p^2 & 0 & 0 \\ 0 & I_{py}+m_p r_p^2 & 0 \\ 0 & 0 & I_{pz}\end{bmatrix}$$

Solving for and rearranging (14) yields (15), which describes the torques acting on the pendulum about its forward axis during a steady-state banking maneuver. The gravitational and centripetal coefficients of each LHS term are labeled G and C, respectively, for later ease of substitution.

$$\begin{aligned}&\underbrace{\left[I_{pz}-(I_{py}+m_p r_p^2)\right]\omega^2\cos(\phi)\sin^3(\phi)}_{\text{Gyroscopic Coupling } N_p} + \underbrace{m_p r_p g}_{G_p}\sin(\phi+\theta) \\ &\qquad\qquad\qquad\qquad\qquad\qquad \underbrace{\qquad\qquad}_{\text{Gravitational Torque}} \\ &+ \underbrace{m_p r_p R\omega^2\cos(\phi)\sin(\phi)}_{C_p}\cos(\phi+\theta) = \underbrace{-\tau_s}_{\text{Actuator Torque}} \\ &\underbrace{\qquad\qquad\qquad\qquad\qquad\qquad}_{\text{Centripetal Torque}}\end{aligned} \tag{15}$$

D. Combination of Moment Equations

As previously discussed, the steering actuator applies a torque τ_s to the shell, with an equal and opposite reaction torque $-\tau_s$ acting on the pendulum. At steady state, τ_s serves as a linking variable, allowing (13) to be substituted into (15), yielding the combined form in (16). This formulation enables a closed-form solution for the pendulum angle θ as a function of the robot's roll angle ϕ, drive shaft speed ω, and internal shell pressure P.

$$\begin{aligned}&G_p\sin(\phi+\theta) + C_p\cos(\phi+\theta) \\ &\quad = -T_{\text{shell}}(\phi,\omega,P) - N_p\end{aligned} \tag{16}$$

Throughout (13) and (15), all velocity-dependent torque contributions have been identified and labeled. These terms are plotted in Fig. 9 to illustrate how their relative magnitudes evolve at three representative drive shaft speeds: 0, 3, and 6 rad/s. Also shown is the shell's flat-induced torque, τ_{flat}, modeled using the empirical formulation presented in [6]. Since τ_{flat} is speed-invariant, it is plotted at an internal pressure of approximately 2 psi, which is the lowest tested pressure from [6] where this effect is most pronounced.

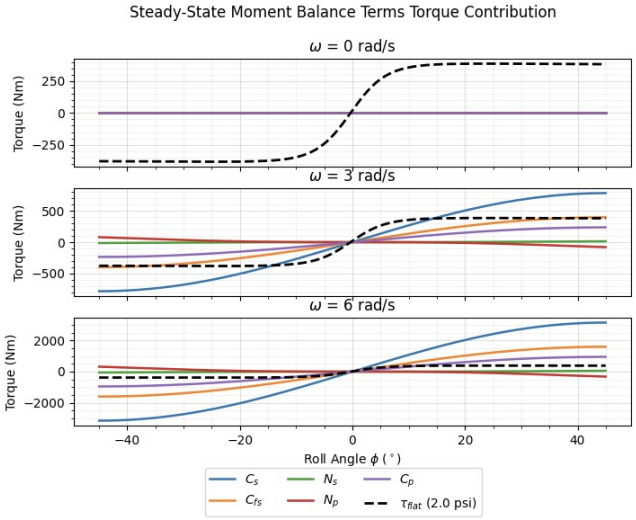

Fig. 9. The torque contribution of each velocity-dependent term compared to the shell's flat induced torque at three distinct drive velocities.

As shown in Fig. 9, the centripetal and centrifugal torque components acting on the shell, C_s and C_{fs} respectively, grow rapidly with increasing ω and begin to dominate all other contributions. At 6 rad/s, these dynamic terms exceed τ_{flat} by over an order of magnitude. This analytic result reinforces the observation that at higher operating speeds, inertial effects, particularly centripetal loading, become dominant drivers of the robot's steering dynamics, surpassing contributions from gravitational loading and material-induced flat torque.

IV. Steady-State Banking Stability Analysis

Equation (16) can be expressed as the trigonometric identity defined in (17), with θ_g defined in (1), and is the angle the pendulum makes with the global vertical axis, called the global pendulum angle.

$$G_p\sin(\theta_g) + C_p\cos(\theta_g) = T_p\sin(\theta_g+\delta) \tag{17}$$

where

$$T_p = \sqrt{G_p^2+C_p^2}, \quad \delta = \tan^{-1}\left(\frac{C_p}{G_p}\right)$$

Solving the trigonometric identity for the global pendulum angle θ_g yields the closed-form expression presented in (18). Fig. 10 visualizes θ_g computed from this expression over roll angles in the range $[-45°, 45°]$ and drive shaft velocities from -10 to 10 rad/s, using parameters specific to RoboBall II. As drive speed increases, the set of roll angles that can be sustained in steady state diminishes—limiting the robot's achievable turning radius.

$$\begin{aligned}\theta_g &= \sin^{-1}\left(\frac{-T_{\text{shell}}(\phi,\omega,P)-N_p}{T_p}\right) - \delta \\ \theta_g &= \sin^{-1}\left(\frac{T_{\text{shell}}(\phi,\omega,P)+(I_{pz}-I_{py})\omega^2 c\phi s^3\phi}{-m_p r_p\sqrt{g^2+(\omega^2 Rc\phi s\phi)^2}}\right) \\ &\quad - \tan^{-1}\left(\frac{\omega^2 Rc\phi s\phi)}{g}\right)\end{aligned} \tag{18}$$

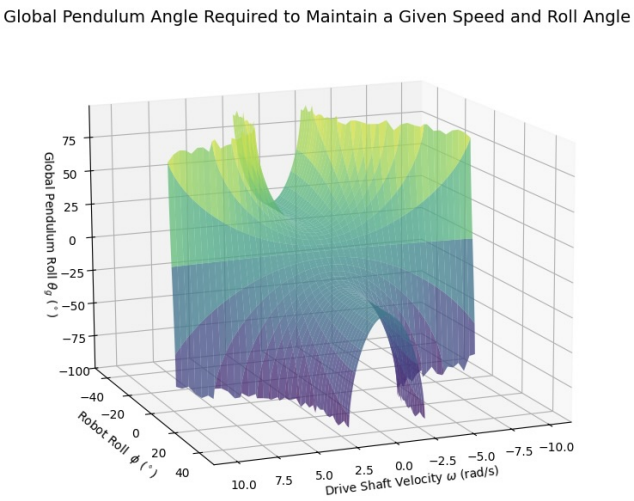

Fig. 10. The global pendulum angle required to maintain banking as a function of drive shaft speed and roll angle. Higher speeds demand greater pendulum authority and reduce available roll range.

At higher speeds, large roll commands become physically infeasible. For example, at 6 rad/s, a commanded roll of 15° may be unsustainable because no pendulum angle θ_g can generate sufficient torque about the steering axis to maintain it. While the steering actuators may be capable, the *actualizable* steady-state torque is bounded by the pendulum's maximum angle ($\theta_g = \pm 90°$), which is further constrained by mechanical interference—namely, the pendulum colliding with the driveshaft—preventing full-range motion.

A. Banking Maneuver's Relationship to Slope Climbing

The Bridgwater Equation (19), introduced in [8], defines the maximum climbable slope angle α as a function of the pendulum pitch angle γ, reaching a maximum at $\pm 90°$ [9]. This can be viewed as the shell effectively *pitching* to align with the slope as it moves uphill. Beyond certain slope angles, determined by the robot's parameters, steady-state climbing becomes infeasible. This concept parallels the Banking Equation (16): whereas the Bridgwater Equation prescribes γ for sustaining a slope, the Banking Equation defines the required pendulum roll angle θ to maintain a steady-state turn for a given roll ϕ and drive speed ω.

$$\sin(\alpha) = \frac{R_{\max}}{R}\sin(\gamma) = \frac{m_{pc}r_{pc} + m_p r_p}{(m_s + m_{pc} + m_p)R}\sin(\gamma) \quad (19)$$

B. Maximum achievable roll angle

Substituting (1) into (18) produces an expression for the steady-state relative pendulum angle θ, which is directly measurable on RoboBall II using an absolute encoder mounted along the steering axis. This pendulum angle, required to maintain a banking maneuver at a given speed, is computed via (18) and plotted in Fig. 11.

The physical limitation of the system imposes a maximum allowed pendulum angle of $\theta_{\text{strike}} = 60°$, beyond which the pendulum would collide with the drive shaft. Since (18) solves directly for θ rather than the roll angle ϕ, a maximum

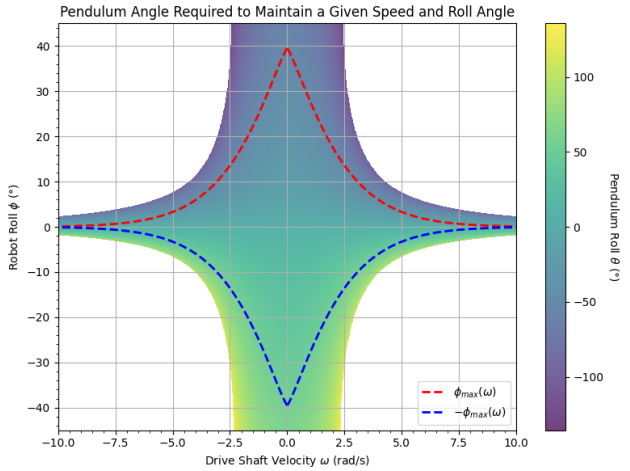

Fig. 11. The relative pendulum angle required to maintain banking with a maximum allowable roll angle function $\phi_{max}(\omega)$.

feasible roll angle, denoted $\phi_{\max}$, must be back-solved to satisfy two key criteria:

1) The resulting pendulum angle must remain below 50°, providing a safety margin to avoid a driveshaft and pendulum collision due to overshoot or transient motion.
2) The magnitude of the pendulum angle gradient, $\|\nabla\theta\|$, must remain below a reasonable threshold to ensure smooth and controllable dynamics (i.e. $\|\nabla\theta\| \leq 0.2$).

As shown in Fig. 10, the gradient of the pendulum angle becomes increasingly steep with higher speeds, indicating that the pendulum's ability to modulate the shell's roll decreases with velocity. By applying the above constraints across the velocity range, a speed-dependent roll angle limit $\phi_{\max}(\omega)$ is obtained and plotted in Fig. 11. This limit is empirically fit using least-squares regression and is described by (20).

$$\phi_{\max}(\omega) = 0.689\, e^{-0.3505\,\omega^{1.216}} - 0.00041 \quad (20)$$

V. Banking Compensated Controller Design

The RoboBall II's steering control law, defined in (21) and visualized in Fig. 12, adopts the full-state feedback (FSF) structure from [6], using the error vector $\vec{\mathbf{e}}_s$ and an LQR-derived gain vector $\vec{\mathbf{K}}_s$ based on the stationary linear model from [7]. The centripetal feedback term τ_{cent} mitigates a speed-induced wobble that emerges near 5.7 rad/s, extending stable operation up to 8 rad/s. The banking compensation torque τ_{bank}, derived from (15), counteracts gravitational and centripetal loads when executing a commanded roll ϕ_{CMD} at drive speed ω. This term implicitly incorporates the soft-shell torque compensation strategy from [6] through the use of θ_{CMD}.

$$\tau_s = \vec{\mathbf{K}}_s \vec{\mathbf{e}}_s + \tau_{\text{cent}} - \tau_{\text{bank}} \quad (21)$$

where

$$\vec{\mathbf{e}}_s = \vec{\mathbf{x}}_{s,CMD} - \vec{\mathbf{x}}_s = \begin{bmatrix} \int(\phi_{CMD} - \phi)dt \\ \phi_{CMD} - \phi \\ \dot{\phi}_{CMD} - \dot{\phi} \\ \theta_{CMD} - \theta \\ \dot{\theta}_{CMD} - \dot{\theta} \end{bmatrix}$$

$$\vec{\mathbf{K}}_s = \begin{bmatrix} k_\Phi & k_\phi & k_{\dot{\phi}} & k_\theta & k_{\dot{\theta}} \end{bmatrix}$$

$$\tau_{\text{cent}} = (m_s + m_{pc} + m_p)R^2 \cos(\phi)\sin(\phi)\omega^2$$

$$\tau_{\text{bank}} = m_p r_p g \sin(\phi_{CMD} + \theta_{CMD}) + N_p(\phi_{\text{CMD}}, \omega) + C_p(\phi_{CMD}, \omega)\cos(\phi_{CMD} + \theta_{CMD})$$

A. Banking Compensation Command Augmentation

As shown in Section IV-A, maintaining a steady-state banking maneuver requires a nonzero pendulum angle θ that depends on the roll angle ϕ, drive shaft speed ω, and internal pressure. The commanded pendulum angle θ_{CMD} in (21) is computed using (18), substituting ϕ with the commanded roll angle ϕ_{CMD}. This ensures the full-state feedback (FSF) setpoint vector $\vec{\mathbf{x}}_{s,\text{CMD}}$ reflects the physical states required for a stable turn.

To prevent instability from infeasible commands, the robot employs the Banking Compensation Command Augmentation System (CAS), detailed in Algorithm 1. CAS computes roll and pendulum angle limits $(\phi_{\max}, \theta_{\max})$ based on the current speed and desired roll angle ϕ_d, using the empirical flat torque model from [6]. If the desired states (ϕ_d, θ_d) exceed these bounds—visualized in Fig. 11—the CAS clamps the commands to stay within the stable region. The final-state commands $(\phi_{CMD}, \theta_{CMD})$ are passed through real-time quintic filters, ensuring C^4-continuous position and C^3-continuous velocity profiles over a 1-second time horizon Δt.

Algorithm 1 Banking Compensation CAS

$\phi_{\max} \leftarrow a\, e^{-b\omega^c} + d$ ▷ from `max_bank_coeffs`
$\theta_{\max} \leftarrow |\,\text{ComputePendAngle}(\omega,\ \phi_{\max},\ \tau_{\text{flat,max}})\,|$
$\tau_{\text{flat,max}} \leftarrow \text{ComputeFlatTorque}(\phi_{\max}, P)$
$\tau_{\text{flat}} \leftarrow \text{ComputeFlatTorque}(\phi_d, P)$
$\theta_d \leftarrow \text{ComputePendAngle}(\omega,\ \phi_d,\ \tau_{\text{flat}})$
if $\theta_d \geq \theta_{\max}$ **then**
    $\theta_{CMD} \leftarrow \theta_{\max}$
    $\phi_{CMD} \leftarrow -\phi_{\max}$
else if $\theta_d \leq -\theta_{\max}$ **then**
    $\theta_{CMD} \leftarrow -\theta_{\max}$
    $\phi_{CMD} \leftarrow \phi_{\max}$
else
    $\theta_{CMD} = \theta_d$
    $\phi_{CMD} = \phi_d$
end if
$\phi_{CMD}, \dot{\phi}_{CMD} \leftarrow \text{QuinticFilter}(\phi_{CMD},\ \phi,\ \dot{\phi},\ \Delta t)$
$\theta_{CMD}, \dot{\theta}_{CMD} \leftarrow \text{QuinticFilter}(\theta_{CMD},\ \theta,\ \dot{\theta},\ \Delta t)$

VI. Experimental Validation

The control law incorporating the banking compensation term and the Command Augmentation System (CAS) for generating feasible trajectories was experimentally validated on the RoboBall II platform, performing banking maneuvers at various speeds. Tests were conducted outdoors on a concrete surface that included small pebbles, minor cracks, and slight unevenness.

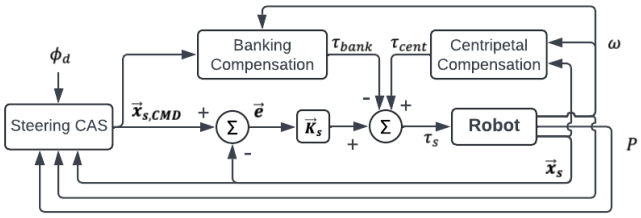

Fig. 12. RoboBall's banking compensated controller design that utilizes the steering command augmentation system (CAS) and banking compensation with the soft-shell compensated controller from [6] incorporated into the banking compensation term.

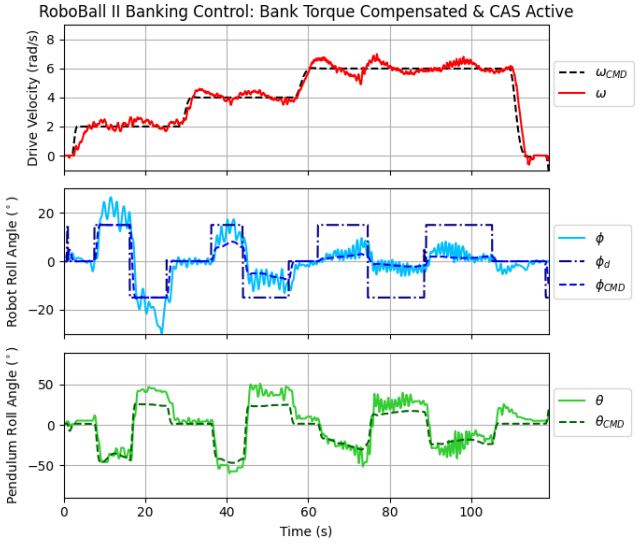

Fig. 13. The measured drive velocity and steering states of RoboBall II during a bank maneuver using the bank-aware controller defined in (21) and the Command Augmentation System (CAS) was active.

Fig. 13 shows RoboBall II's measured drive velocity and steering states during a bank maneuver using the bank-aware controller from (21) and the CAS strategy from Algorithm 1. While low-speed maneuvers at 2 rad/s (0.61 m/s) exhibit some overshoot, the robot remains stable and predictable at higher speeds. Although the commanded roll angle ϕ_{CMD} is reduced compared to the desired ϕ_d, the robot still achieves effective bank maneuvers while preserving stability at 6 rad/s (1.83 m/s).

Fig. 14 shows RoboBall II's drive velocity and steering states during a bank maneuver using the soft-shell-compensated controller from [6] with centripetal torque feedback [7], but without bank compensation or CAS. The controller tracks $\pm 15°$ roll commands well at 2 rad/s, struggles at 4 rad/s, and becomes unstable at 6 rad/s, ultimately causing the robot's stability to become unrecoverable and result in the robot flipping end-over-end.

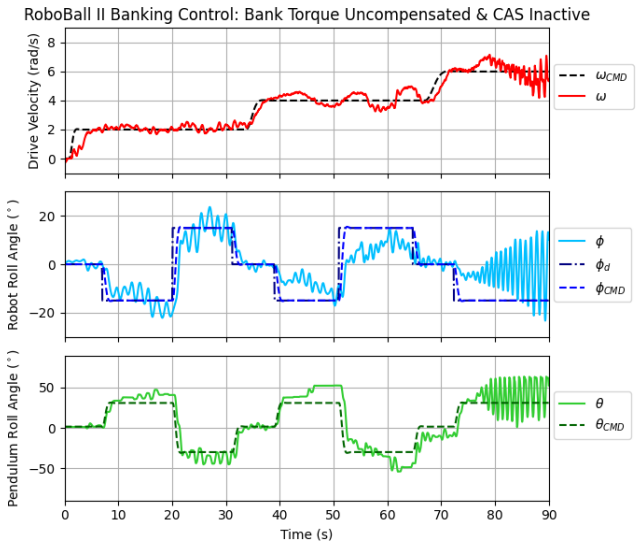

Fig. 14. The measured drive velocity and steering states of RoboBall II during a bank maneuver using the soft-shell-compensated controller from [6] with centripetal torque feedback from [7] enabled. Neither the bank compensation nor the Command Augmentation System (CAS) were active during this test.

VII. Conclusion

This work presented a Command Augmentation System (CAS) for pendulum-driven spherical robots that enables stability-aware steering through dynamic roll angle constraints. A closed-form solution for the required pendulum angle under steady-state banking was derived by balancing centripetal, gravitational, and shell flat torques, revealing how centripetal loading increases with drive speed. This growth in dynamic loading demands increasingly aggressive pendulum actuation, ultimately imposing physical limits on feasible roll angles. By embedding this model into both the control law and the CAS, the robot is able to avoid unstable regimes in real time. Experimental results confirm this: without banking compensation or CAS, the robot becomes unstable during sharp banked turns at 6 rad/s, while the bank-aware controller with CAS maintains stability and enables meaningful maneuvers at all tested speeds.

Future work will extend this CAS framework by incorporating automatic deceleration, allowing the robot to reduce speed to remain within its safe banking envelope. Specifically, when the CAS's clamp is triggered, the commanded roll angle ϕ_{CMD} will be modified as described in this paper, while the drive shaft speed command ω_{CMD} will also be reduced to ensure that the operator's desired roll angle ϕ_d becomes feasible without violating stability constraints. This would be the equivalent of the commanded roll and drive velocity states *glide* along the maximum roll function $\phi_{max}(\omega)$ depicted in Fig. 11. This behavior mimics that of conventional ground vehicles, which typically must decelerate before sharp turns, but the operator does not need to concern themselves with avoiding instability, but rather regaining the higher speed agility that was lost during this work's validation campaign.

In addition to software enhancements, the proposed CAS will be implemented on a significantly larger platform: RoboBall III. This robot features a 1.83 m diameter and a mass of 155 kg. While it offers a larger roll angle range compared to RoboBall II, its altered physical parameters result in different torque and pendulum angle requirements for maintaining speed during banked turns. This presents an opportunity to explore scalable, parameterized control laws that generalize across soft-shell spherical robots of varying sizes and inertial properties.

References

[1] C. A. Anderson. "Development of an active fly-by-wire flight control system". In: *NASA Dryden Flight Research Center Advanced Control Technology and its Potential for Future Transport Aircraft*. Conference Paper, Document ID: 19760024050, Accession Number: 76N31138. Edwards, CA: NASA, 1976.

[2] Ziang Zhang et al. "Improved hybrid A* path planning method for spherical mobile robot based on pendulum". In: *International Journal of Advanced Robotic Systems* 18.1 (2021), p. 1729881421992958. DOI: 10.1177/1729881421992958. eprint: https://doi.org/10.1177/1729881421992958. URL: https://doi.org/10.1177/1729881421992958.

[3] Masaki Nagai. "Control System for a Spherical Robot". In: Masters Thesis. 2008.

[4] Bruno Belzile and David St-Onge. "Design and Modeling of a Spherical Robot Actuated by a Cylindrical Drive". In: *2022 IEEE International Conference on Robotics and Automation (ICRA)*. May 2022, pp. 1169–1175. DOI: 10.1109/ICRA46639.2022.9812148.

[5] Affiani Machmudah et al. "Flight Trajectories Optimization of Fixed-Wing UAV by Bank-Turn Mechanism". In: *Drones* 6.3 (2022). ISSN: 2504-446X. DOI: 10.3390/drones6030069. URL: https://www.mdpi.com/2504-446X/6/3/69.

[6] Derek J. Pravecek. "Empirically Compensated Setpoint Tracking for Spherical Robots With Pressurized Soft-Shells". In: *IEEE Robotics and Automation Letters* 10.3 (2025), pp. 2136–2143. DOI: 10.1109/LRA.2025.3527308.

[7] Derek J. Pravecek. "Dynamic Analysis and Stabilization of Speed-Dependent Wobble Induced by Centripetal Coupling in Pendulum-Driven Spherical Robots". In: (). progress.

[8] Lyndon B. Bridgwater. "RoboBall: Lightweight Martian Rover Concept". In: *Space Technology and Applications International Forum (STAIF)*. 2008.

[9] Rishi V. Jangale. "Scaling of RoboBall: A Parametric Robot Family for Crater Exploration". In: *2025 IEEE Aerospace Conference*. 2025. DOI: 10.1109/AERO63441.2025.11068434.